PAPER

Check for updates

Silica template-assisted synthesis of SnO2@porous carbon composites as anode materials with excellent rate capability and cycling stability for lithium-ion batteries†

Jian Guo, Ping Li, Liying Chai, Yi Su, Jinxiang Diao and Xiaohui Guo (ID) *

In this study, a type of porous carbon-coated SnO_2 nanoparticle composite (SnO_2@PC) was produced in the presence of a silica template. The prepared SnO_2@PC composite displays a highly specific surface area (SSA) and large pore volume compared with common porous carbons. Electrochemical testing demonstrates that as an anode material the SnO_2@PC1 composite can deliver a specific capacity of 1130.1 m Ah g^{-1} at a current density of 0.2 A g^{-1} after 100 cycles, which is much higher than that of pure SnO_2 anodes. The specific capacity of the SnO_2@PC1 anode is as high as 770.3 m Ah g^{-1} at a current density of 0.5 A g^{-1} after 300 cycles, indicating excellent rate and cycling capability. The superior lithium storage performance of the SnO_2@PC1 composite can be attributed to the synergistic effect of the porous carbon and SnO_2 nanoparticles. In addition, the large specific surface area and pore volume of the SnO_2@PC1 composite can significantly shorten the diffusion path of lithium ions and provide a sufficient internal void space for volume change. The proposed synthetic approach is facile, controllable, and economical, and can be applied in producing carbon coatings for other transition metal oxide-based composite functional materials.

1. Introduction

Lithium-ion batteries (LIBs) have attracted a great deal of attention as popular energy storage devices due to their excellent electrochemical performance, such as having a long cycle lifetime and high energy density.[1–3] Anode materials in LIBs play a key role in modulating the lithium storage performance. Graphite, as the traditional LIB anode material, cannot meet our daily demands owing to its low theoretical specific capacity of only 372 m Ah g^{-1}.[4,5] The development of electronic devices has presented higher energy storage requirements for LIBs. Hence, the exploitation of advanced anode materials with excellent lithium storage capabilities has become very urgent.

Currently, SnO_2 is considered as one of the most promising anode materials for next-generation LIBs due to several unique characteristics including a high theoretical capacity (*ca.* 790 m Ah g^{-1}), environmental friendliness, natural abundance, and a low cost. However, the sizable volume expansion/contraction associated with lithium insertion/extraction causes the destruction and collapse of the SnO_2 anode structure, which

further causes severe capacity fading and poor cycling stability.[6–8] These disadvantages have severely restricted the practical application of SnO_2 in LIBs.

To our knowledge, many research groups have attempted to develop high-performance SnO_2-based anode materials with high cyclic stability for next-generation LIBs. Compared to bulk SnO_2 materials, nanostructured SnO_2 materials have been proven to be effective in buffering the volume change of SnO_2 anodes and shortening the diffusion path of lithium ions.[9,10] SnO_2 structures such as ultrafine SnO_2 nanoparticles,[11] SnO_2 quantum dots,[12] hollow SnO_2 spheres,[13,14] porous SnO_2,[15] SnO_2 nanorods,[16] SnO_2 nanotubes,[17–19] SnO_2 nanosheets[20] and SnO_2 nanoribbons[21] have been successfully produced *via* various synthetic approaches in recent studies. However, further improvements in the electrochemical performance of these nanostructured SnO_2 anodes are limited owing to their poor electrical conductivity.

Various conductive components such as MoS_2,[22] conductive polymers,[23–25] and conductive carbon materials (including graphene,[26–28] carbon nanotubes,[29,30] carbon nanofibers,[31–34] and 3D carbon frameworks[35–37]) have been introduced into SnO_2 materials to enhance their electrical conductivity and accelerate ion transfer. These conductive matrices can effectively accommodate the internal stress caused by the SnO_2 volume change during the charge/discharge process, which can prevent the aggregation of SnO_2 nanoparticles[27] and hence improve the

Key Lab of Synthetic and Natural Functional Molecule Chemistry of Ministry of Education, The College of Chemistry and Materials Science, College of Chemistry and Materials Science, Northwest University, Xi'an 710069, China. E-mail: guoxh2009@nwu.edu.cn; Tel: +86-2981535025

cyclic stability of the SnO_2 materials. Although improved cyclic durability has been realized for these SnO_2-based composite anodes, the issue of fast capacity decay at high rates still limits the scalable application of SnO_2-based composite anodes in LIBs.

Among these conductive materials, porous carbon materials have attracted extensive interest due to their high specific surface area, low density, large pore volume, and high mass loading, so they would be an ideal support for SnO_2 nanoparticles with regard to their electrochemical performance in LIBs. The lithium storage properties of carbon-coated SnO_2 (SnO_2@PC) composites can be significantly improved by integrating a porous carbon coating layer wherein large amounts of active sites for lithium storage are supplied by the large specific surface area (SSA), which can increase the contact area with the electrolyte. The hollow internal structure provides extra void space to accommodate the structural strain and volume expansion, which can assure the integrity of the electrode structures.[35] The pulverization and agglomeration of the SnO_2 nanoparticles is also prevented by adding a porous carbon coating layer,[36] additionally, alloying and dealloying during the charge/discharge processes is effectively modulated *via* a desirable porous channel that favors the reversibility of the electrochemical reaction. These excellent porous features would ensure the realization of high capacity retention at high rates or long-term cycling.

Recently, various SnO_2@porous carbon-based anode architectures have been developed to provide enhanced electrochemical performance in LIBs. For example, Zhou *et al.* prepared SnO_2 quantum dots encapsulated by a three-dimensional porous carbon network ($NSGC$@SnO_2) based anode material, which can deliver a specific capacity of 1118 m Ah g^{-1} at a current density of 0.2 A g^{-1} after 100 cycles.[38] Chen *et al.* synthesized ultrafine SnO_2 nanoparticles embedded in carbon networks as an anode material that can exhibit a discharge specific capacity of 597.3 m Ah g^{-1} at a current density of 0.1 A g^{-1} after 220 cycles.[39] Jin *et al.* reported that SnO_2 nanoparticles@CMK-3 composite-based anodes can deliver a discharge specific capacity of 1054 m Ah g^{-1} at a current density of 0.1 A g^{-1}.[40] Although the electrochemical performance of the above mentioned SnO_2@porous carbon-based anodes has been improved in LIBs, their absolute electrochemical capacity remains unsatisfactory and still suffers capacity decay during the initial ten or twenty cycles. In other words, the fabrication of SnO_2@porous carbon composite electrode materials with simultaneous high rate capability and stable cycling performance remains elusive. Moreover, the synthetic processes involved in obtaining such composites are relatively complex, thus limiting their large-scale applications in LIBs. As a result, there is sizable demand for producing high-performance SnO_2@porous carbon composite anodes *via* a facile and economical synthetic approach.

In this work, we synthesized a type of porous carbon-coated SnO_2 (SnO_2@PC) based composite with the assistance of a silica template under mild conditions. The PC was generated by a facile sol–gel route followed by a calcination treatment process. The prepared SnO_2@PC1 composite displayed a high specific surface area of 246.2 m^2 g^{-1} and a large pore volume of 0.505 cm^3 g^{-1}. Due to the synergic effect of the SnO_2 nanoparticles and the porous carbon network, as an advanced anode material the prepared SnO_2@PC1 composite delivers an initial specific capacity of 1803 m Ah g^{-1}, remarkable cycling stability and outstanding rate capability. More importantly, the unique porous carbon-coated metal oxide-based composite structure could possess potential applications in chemical, adsorption, catalytic, and biological engineering fields.

2. Experimental section

Analytical grade tin(IV) chloride pentahydrate ($SnCl_4 \cdot 5H_2O$), sodium hydroxide (NaOH), concentrated hydrochloric acid (HCl, 37 wt%), glucose and sodium silicate ($Na_2SiO_3 \cdot 9H_2O$) were used without any further purification.

2.1 Synthesis of SnO_2@PC

First, the SnO_2 nanoparticles were produced according to a previously reported synthetic method.[41] Then, SnO_2@PC1 was synthesized by the following procedures. 0.5 g of SnO_2 NPs was dispersed in 25 mL of water by ultrasonic treatment for 2 h, and then 1 mL of concentrated hydrochloric acid, 0.4 g of glucose and 2.4 g of sodium silicate were added into the above suspension under vigorous stirring. A gel-like product was formed several minutes later and subsequently dried in air at 80 °C in an oven overnight. The resulting product was ground into a powder and transferred to a corundum crucible. The corundum crucible was put into a tubular furnace under a N_2 atmosphere and heated to 550 °C with a ramp rate of 5 °C min^{-1}. After it cooled to room temperature, the resulting powder was etched in a hydrofluoric acid solution, followed by washing with water and ethanol several times. Finally, the product was obtained *via* drying treatment in an oven at 80 °C for 5 h. For comparison, SnO_2@PC2 (0.3 g glucose), SnO_2@PC3 (0.5 g glucose), and SnO_2@PC4 (0.1 g glucose) samples were synthesized by a similar synthetic procedure, only changing the weight of glucose. In addition, SnO_2@C was synthesized by a similar procedure without the addition of hydrochloric acid and sodium silicate.

2.2 Characterization

The morphology and crystal structures of all the samples were characterized by a field-emission scanning electron microscope (FE-SEM, Hitachi, S-4800), a high-resolution transmission electron microscope (HRTEM, FEI Tecnai G2 F20) and a Bruker D8 advance X-ray powder diffractometer. The surface electron state of SnO_2@PC1 was identified by an X-ray photoelectron spectroscope (XPS, Model VG ESCALAB). The specific porous structures of all the samples were determined by a Brunauer–Emmett–Teller (BET) surface analyzer (Tri Star-3020, Micromeritics, USA). Component identification of the samples was performed *via* a Raman spectrometer (Jobin Yvon Co., France) model HR800 employing a 10 mW helium/neon laser at 632.8 nm. The carbon content in the samples was measured *via* thermogravimetric analysis (TGA, Netzsch-Sta 449) in an air

atmosphere, over a temperature range of 25–1000 °C with a heating rate of 10 °C min^{-1}.

2.3 Electrochemical performance evaluation

CR2032 coin-type cells were used to test the electrochemical performance of all the samples. The working electrode was prepared by mixing the synthesized materials, acetylene black and sodium alginate at a weight ratio of 7 : 1.5 : 1.5 in a water solvent. The obtained slurry was cast on Cu foil and dried under vacuum at 80 °C for 8 h. The electrode was cut into circular disks of 12 mm with an average mass loading of 0.8 mg cm^{-2}. The LIBs were assembled in an argon-filled glove box. 1 M LiPF$_6$ in ethylene carbonate (EC) and diethyl carbonate (DEC) (1 : 1, v/ v) was used as the electrolyte, Celgard 2400 microporous polypropylene membrane as the separator and Li foil as the counter electrode. The electrochemical properties of the assembled cells were measured by a LAND-CT2001A battery test system within a voltage range of 0.005 to 3 V. Cyclic voltammetry (CV) was carried out by a CHI660e electrochemical workstation at a scan rate of 0.2 mV s^{-1} within a voltage window of 0.005 to 3 V (vs. Li/Li$^+$).

3. Results and discussion

The SnO$_2$@PC fabrication procedure is illustrated schematically in Fig. 1. The three SnO$_2$-based samples were obtained via a facile synthetic approach, as described above. The structural features of the SnO$_2$ nanoparticles, SnO$_2$@C, and SnO$_2$@PC1 were characterized by XRD. As shown in Fig. 2a, the diffraction peaks of the three samples correspond to those of rutile SnO$_2$ (JCPDS card no. 41-1445), while the main diffraction peaks at 26.6°, 33.8°, 37.9°, 51.8°, and 54.8° are ascribed to (110), (101), (200), (211), and (220) facets, respectively, indicating the good crystalline nature of the SnO$_2$ component. The broad peak at 20–25° can be ascribed to the amorphous carbon.[40] In contrast to the XRD patterns of pure SnO$_2$, no other impurity peaks were detected in the XRD patterns of SnO$_2$@PC1 or SnO$_2$@C. By comparison, SnO$_2$@PC2, SnO$_2$@PC3, and SnO$_2$@PC4 samples were produced by modulating the glucose content in the same reaction system. These samples displayed similar structure and morphology features to SnO$_2$@PC1 (Fig. S1†).

The morphologies of SnO$_2$@PC1 and SnO$_2$@C were observed via FESEM, and it was found that the SnO$_2$@C displays a large aggregate structure, which is approximately several microns in size (Fig. 2b). The SnO$_2$@PC1 presents a porous, network-like structure with many interconnected pores. The SnO$_2$ nanoparticles are uniformly coated with a carbon layer, exhibiting a marked difference compared with the SnO$_2$@C (Fig. 2c–d). TEM was performed to further observe the microstructure of the SnO$_2$@PC1 (Fig. 2e–f). The SnO$_2$ nanoparticles were uniformly anchored on a porous carbon framework and had a mean size of about 10–20 nm, as shown in Fig. 2f. The SnO$_2$ nanoparticles displayed well-defined crystal lattice stripes, and the spacing was measured to be 0.33 nm, corresponding to the (110) plane. The components of the SnO$_2$@PC1 sample were also confirmed via EDS analysis, as shown in Fig. 2g. The sole presence of C, O,
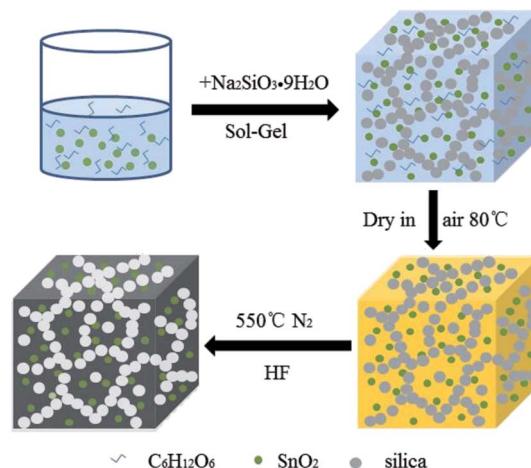

Fig. 1 A schematic illustration of the synthesis of SnO$_2$@PC.

and Sn in the sample indicates the successful formation of a carbon-coated SnO$_2$-based composite.

In order to confirm the presence of a carbon component in the sample, Raman spectroscopy was performed at room temperature, as shown in Fig. 3a. The SnO$_2$@PC1 displays two broad peaks at about 1350 and 1591 cm^{-1}, assigned to the D band and G band, respectively, which are characteristic of carbon species.[42] The peak intensity ratio between the D band and G band ($I_D/I_G \sim 0.837$), indicates high defect concentrations in the porous carbon. In addition, the carbon content of the four SnO$_2$@PC-based samples was quantified via TGA testing, and the corresponding carbon content in SnO$_2$@PC1, SnO$_2$@PC2, SnO$_2$@PC3, and SnO$_2$@PC4 was calculated to be 14.1, 9.3, 15.7, and 2.6 wt%, respectively, as shown in Fig. 3b and S2.†

Isothermal N$_2$ adsorption–desorption analysis was employed to investigate the porous features of SnO$_2$@PC1 and SnO$_2$@C. The N$_2$ adsorption–desorption isotherms acquired at 77 K and the Barrett–Joyner–Halenda (BJH) adsorption pore size distribution plots of the samples are shown in Fig. 4. The nitrogen adsorption isotherms of the samples are typical type IV curves and the loop nature of the nitrogen adsorption isotherms suggests the presence of the mesoporous structure of the samples. According to the corresponding Barrett–Joyner–Halenda (BJH) calculation, the SSA and pore volume of the as-prepared SnO$_2$@PC1 were measured as 246.2 m^2 g^{-1} and 0.505 cm^3 g^{-1}, respectively, and the pore size was focused at 11.8 nm. For comparison, the SSA, pore volume and pore size of SnO$_2$@C were calculated as 83.25 m^2 g^{-1}, 0048 cm^3 g^{-1} and 3.9 nm, respectively. Additionally, we also examined the porous features of the SnO$_2$@PC2, SnO$_2$@PC3, and SnO$_2$@PC4 samples. The obtained N$_2$ adsorption–desorption isotherms and the pore-size-distribution curves of the three SnO$_2$@PC-based samples are shown in Fig. S3.† As a result, it is believed that the larger specific surface area and pore volume of SnO$_2$@PC were generated by removal of the silica template.

To further investigate the state of the elements within the SnO$_2$@PC1, XPS analysis was implemented and the
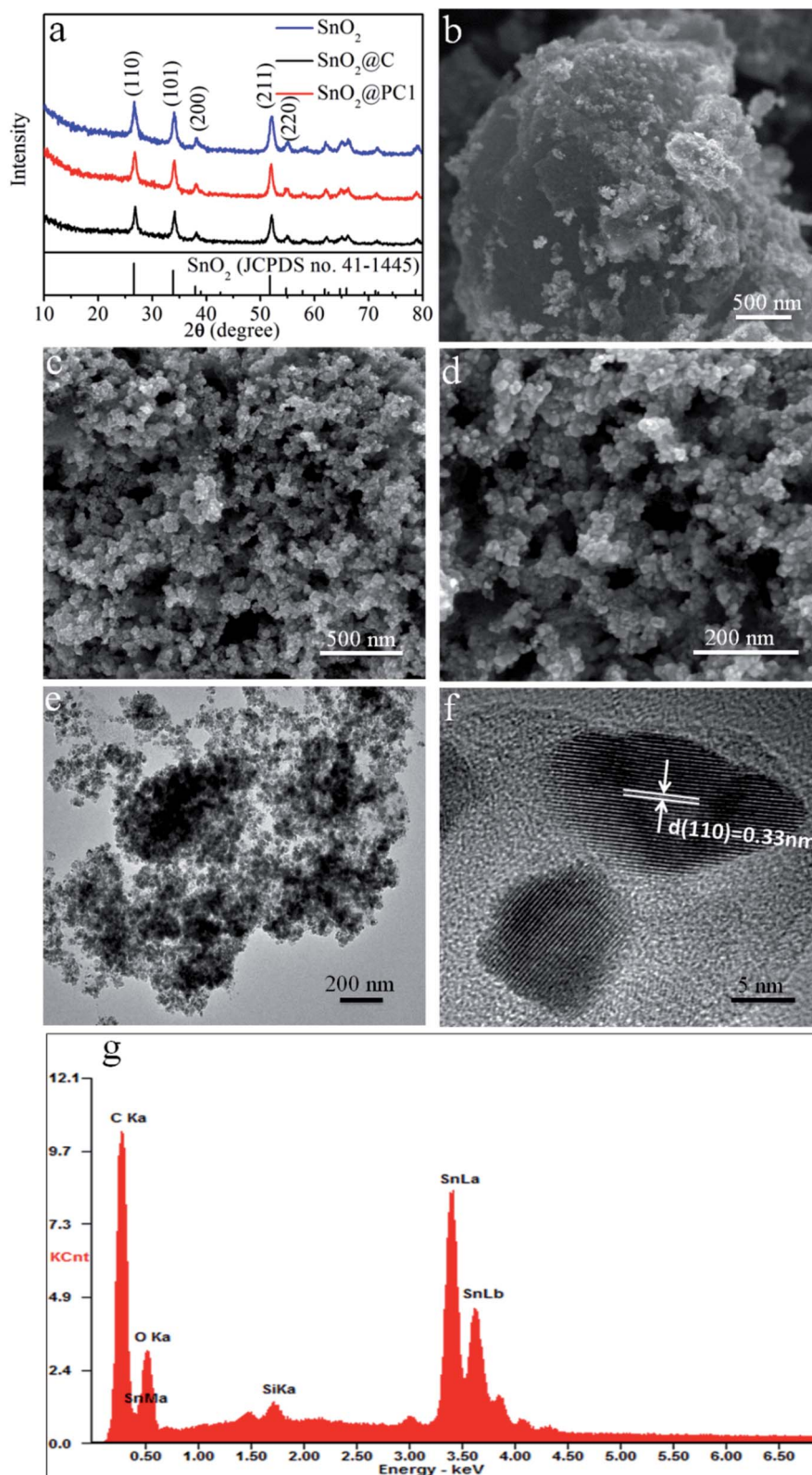
Fig. 2 (a) XRD patterns of SnO$_2$, SnO$_2$@C and SnO$_2$@PC1. (b) FE-SEM images of SnO$_2$@C; (c and d) FE-SEM images of SnO$_2$@PC1 at different resolutions; (e) TEM image and (f) HRTEM image of SnO$_2$@PC1; (g) EDS pattern of SnO$_2$@PC1.

corresponding results are presented in Fig. 5. The survey XPS spectrum of SnO$_2$@PC1 (Fig. 5a) indicates the presence of Sn, O, and C species in the sample. As shown in Fig. 5b, it was seen that three major peaks at binding energies of 285 eV, 286 eV and 287.32 eV are ascribed to the C–C, C–O and C=O bonds, respectively.[40] The XPS spectra of the O 1s species split into
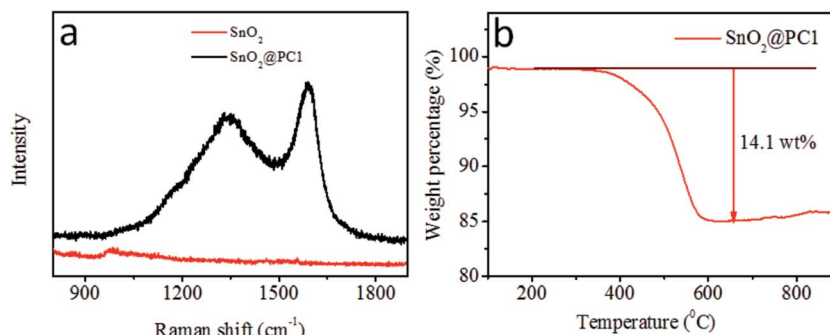
Fig. 3 (a) Raman spectra of SnO_2 and SnO_2@PC1; (b) the TGA curve of SnO_2@PC1.

three distinct peaks centred at binding energies of 531.6, 532.7, and 533.5 eV, corresponding to Sn–O, C=O, and C–O bonds, respectively, indicating the presence of O^{2-} (Fig. 5c). Two peaks at binding energies of 487.6 eV (Sn $3d_{5/2}$) and 496 eV (Sn $3d_{3/2}$) can be clearly seen from the high-resolution Sn 3d XPS spectra, as illustrated in Fig. 5d, which confirms the presence of Sn^{4+} in the sample. These XPS results confirm the presence of SnO_2@PC1.

The electrochemical performance of the bare SnO_2, SnO_2@PC, and SnO_2@C anodes was investigated. The reaction mechanism of the SnO_2@PC1 electrode for the initial several cycles was measured *via* cyclic voltammetry in the voltage range of 0.005–3.0 V (*vs.* Li/Li$^+$) at a scan rate of 0.2 mV s^{-1}, as shown in Fig. 6a. In the first cycle, two cathodic peaks were observed at 0.58 V and 0.06 V. The peak at 0.58 V disappeared in subsequent cycles, corresponding to the formation of an SEI layer, the conversion of SnO_2 into Sn and the formation of amorphous Li_2O, while the peak at 0.06 V is attributed to the formation of Li_xSn. The peaks at 0.4–1 V in the anodic curves are a result of dealloying of Li_xSn, and the anodic peaks at 1.28 and 1.86 V are attributed to the partial oxidation of Sn into SnO_x. Two cathodic peaks can be observed at 0.88 and 1.18 V after the first cycle that correspond to the reduction of SnO_x into Sn, indicating the partial reversibility in eqn (1) that is responsible for the excess capacity. The reduction peak potential is shifted from 0.58 to 1.18 V, suggesting the partial reduction of SnO_x into Sn after the first cycle, which can be confirmed in Fig. S4.† All curves can be overlapped after the first cycle, which indicates the superior reversibility and cycling durability of the SnO_2@PC1

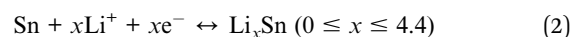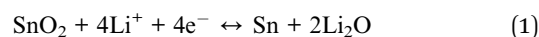electrode.[18,38] The whole reaction process is represented by the following equations:

$$SnO_2 + 4Li^+ + 4e^- \leftrightarrow Sn + 2Li_2O \tag{1}$$

$$Sn + xLi^+ + xe^- \leftrightarrow Li_xSn \ (0 \leq x \leq 4.4) \tag{2}$$

Fig. 6b shows the discharge–charge curves of the SnO_2@PC1 electrode for different cycles at a current density of 0.2 A g^{-1} in the voltage range of 0.005–3.0 V (*vs.* Li/Li$^+$). The first discharge curve of the SnO_2@PC1 electrode exhibited a voltage platform at 0.8 to 1 V that was apparently different from the rest curves, which can probably be ascribed to the formation of an SEI layer and the conversion of SnO_2 into Sn. The charge–discharge specific capacities of the SnO_2@PC1 electrode in the initial cycles were 1255 m Ah g^{-1} and 1803.5 m Ah g^{-1}, respectively. The capacity loss during the first cycle results from the formation of the SEI layer, which is a common phenomenon for most anode materials. The initial capacity is much higher than the theoretical capacity of pure SnO_2 owing to the good reversibility in eqn (1). In addition, the decomposition of the electrolyte in the low-potential region and the simple adsorption of Li$^+$ on the surface of the supporting carbon matrix are also responsible for the enhanced capacity.[43] The discharge–charge curves exhibit little change from the 2nd to the 100th cycle, and then the coulombic efficiency can reach 99%, indicating the excellent reversibility and cycling stability of the SnO_2@PC1 electrode.
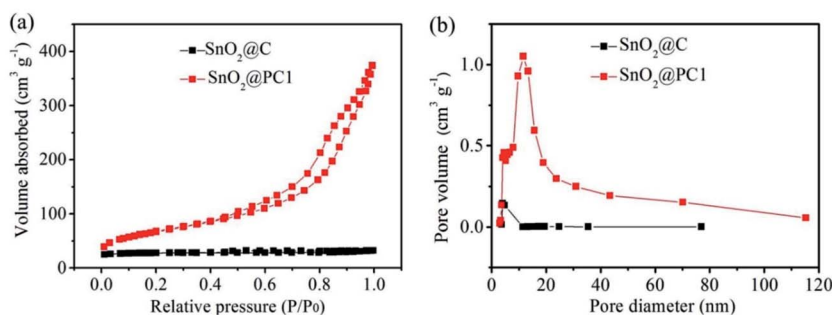

Fig. 4 (a) Nitrogen adsorption–desorption isotherms and (b) pore size distribution plots of SnO_2@C and SnO_2@PC1.
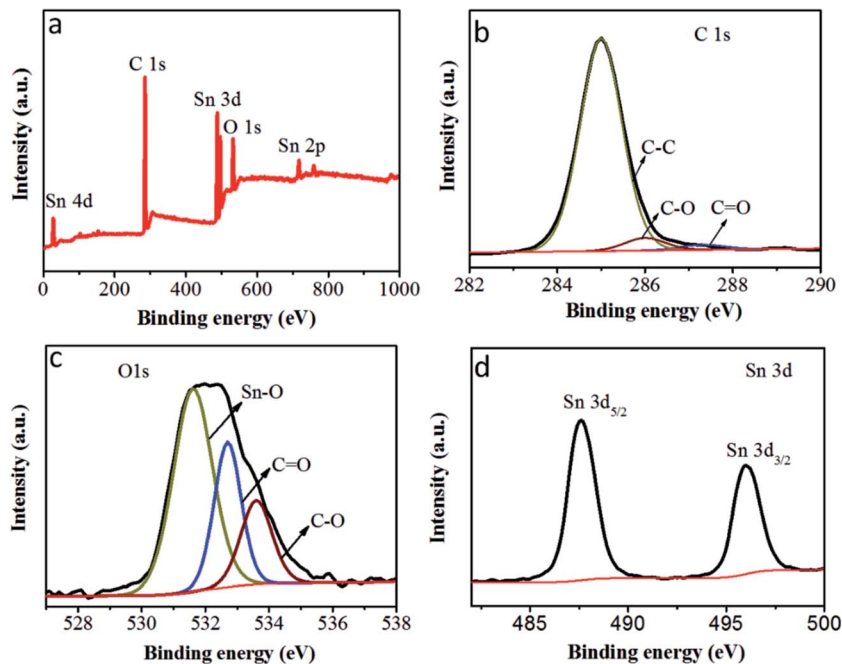
Fig. 5 (a) The XPS survey scan of SnO_2@PC1, (b) the XPS spectra of C 1s peaks of SnO_2@PC1, (c) the XPS spectra of O 1s peaks of SnO_2@PC1 and (d) the XPS spectra of Sn 3d peaks of SnO_2@PC1.

Meanwhile, at the same charge–discharge testing conditions, the initial discharge capacity of the bare SnO_2 anode was 939 m Ah g^{-1}, thus the coulombic efficiency for the first cycle was 62.5%. In the second cycle, it delivered a discharge capacity of 780 m Ah g^{-1} with a coulombic efficiency of 90.7% (Fig.-S5b†), which is in accord with the CV result in Fig. S5a.† Meanwhile, the SnO_2@C electrode exhibited a similar discharge–charge feature with the bare SnO_2 nanoparticles, as shown in Fig. S6.† These results indicate that the bare SnO_2 NPs and SnO_2@C undergo a large capacity loss during the initial discharge–charge cycles, which can probably be ascribed to the formation of unstable SEI film and the irreversibility of the reaction described by eqn (1).

To further study the cycling durability of the three anodes, they were cycled at a voltage window of 0.005 to 3 V under a current density of 0.2 A g^{-1} (results are shown in Fig. 6c). The bare SnO_2 anode delivered a charge specific capacity of 321 m Ah g^{-1} after 100 cycles, with a capacity retention of 47.1%. It was noted that the pure carbon anode delivered a low charge specific capacity of 107.46 m Ah g^{-1} after 50 cycles (Fig. S7†). Moreover, the SnO_2@C anode delivered a charge specific capacity of 414 m Ah g^{-1} after 100 cycles, with a capacity retention of 51.0%. The rapid capacity decay for the pure SnO_2 and SnO_2@C anodes after 100 cycles may have resulted from the electrode structure collapse and pulverization of the SnO_2 active material. In contrast, the SnO_2@PC1 electrode exhibited superior cycling stability compared with SnO_2@C and bare SnO_2. For the SnO_2@PC1 electrode, the charge specific capacity of SnO_2@PC1 after 100 cycles could reach 1130 m Ah g^{-1}, with a capacity retention of 90.0%, which is much higher than that of bare SnO_2 and SnO_2@C. These results demonstrated that the novel porous carbon structures directed by the silica template can effectively enhance the structural stability and cycling performance, which can be evidenced in previous literature.[44]

Herein, the complete carbon enclosure and the large void space between the core and shell can physically restrict the SnO_2 core and buffer its volume expansion, preventing it from pulverization and detaching from the current collector, which can favor a high specific capacity after long-time cycling. It should be noted that the discharge specific capacity of the SnO_2@PC1 electrode can deliver 1130 m Ah g^{-1} at 0.2 A g^{-1} after 100 cycles, which is much higher than the theoretical capacity of SnO_2 ($\sim$790 m Ah g^{-1}). The extra capacity may result from the reversible formation of an organic polymeric gel-like layer caused by electrolyte decomposition at low potential and the electro-catalytic reversible conversion of some components from SEI films.[36,45] The partially reversible conversion between Sn and SnO_x at the initial cycle process can also contribute additional capacity. In addition, previous work also suggested that a nanostructure with a porous structure may improve the number of Li$^+$ storage sites and contribute extra capacity.[46]

The rate performance of the bare SnO_2, SnO_2@C, and SnO_2@PC1 electrodes was investigated at current densities ranging from 0.1 to 3 A g^{-1}. As shown in Fig. 6d, the specific capacities of the bare SnO_2, SnO_2@C, and SnO_2@PC1 anodes at a current density of 0.1 A g^{-1} after 10 cycles were 781, 761, and 1247 m Ah g^{-1}, respectively. As the current density was increased to 0.5 A g^{-1}, the specific capacities of the bare SnO_2, SnO_2@C, and SnO_2@PC1 anodes were 633, 671, and 1039 m Ah g^{-1}, respectively. Further increasing the current density to 3 A g^{-1} gave specific capacities of the bare SnO_2, SnO_2@C, and SnO_2@PC1 anodes of 366, 413, and 692 m Ah g^{-1} after 70 cycles,
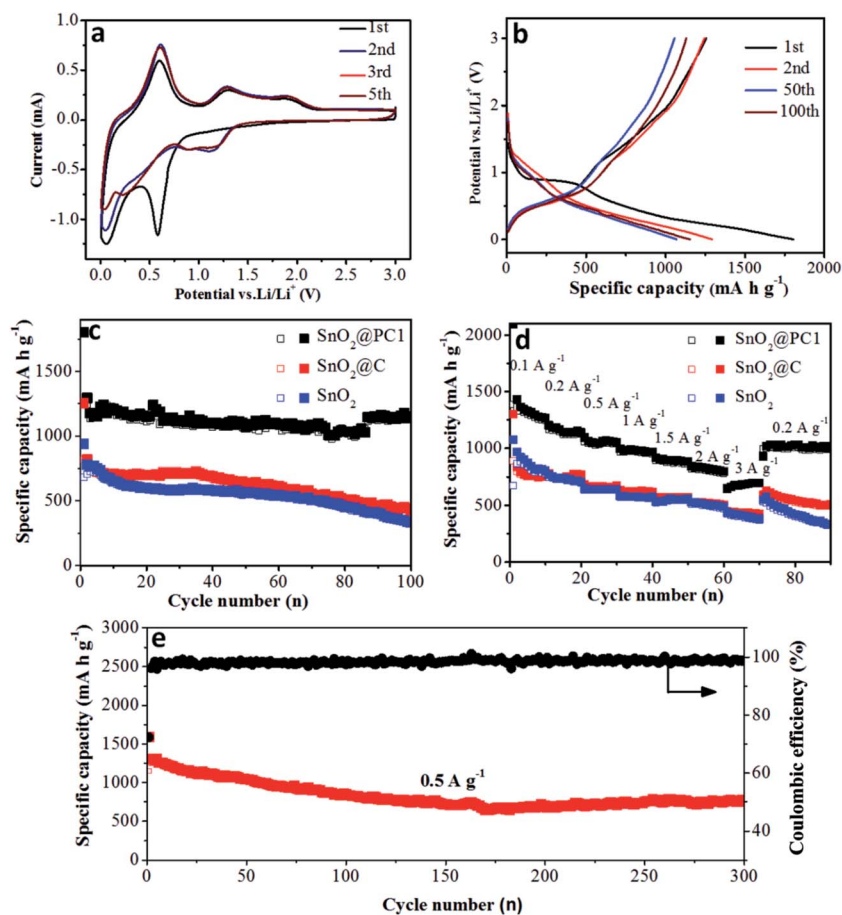
Fig. 6 The electrochemical performance evaluation of bare SnO_2, $SnO_2@C$, and $SnO_2@PC1$ anodes; (a) CV curves of $SnO_2@PC1$; (b) charge/discharge curves of $SnO_2@PC1$; (c) cycling performance curves at 0.2 A^{-1} g; (d) the rate performance of bare SnO_2, $SnO_2@C$; $SnO_2@PC1$ and (e) the long term cycling performance curve of $SnO_2@PC1$ at a current density of 0.5 A^{-1} g.

respectively. The $SnO_2@PC1$ anode was found to retain a relatively high specific capacity of 698 m Ah g^{-1} at high rate testing conditions, which highlights its potential as an advanced anode material for next-generation LIBs. When the current density was returned back to 0.2 A g^{-1}, the specific capacities of the bare SnO_2, $SnO_2@C$, and $SnO_2@PC1$ were 321, 492, and 1002 m Ah

g^{-1}, respectively. The specific capacities of the $SnO_2@C$ and $SnO_2@PC1$ anodes were close to their initial values, implying their excellent rate capability and cyclic reversibility. In addition, electrochemical impedance spectroscopy of the SnO_2-based anodes was conducted, as shown in Fig. S8.† It was found that $SnO_2@PC1$ displays low charge transfer resistance

Table 1 A comparison of the electrochemical properties in $SnO_2@$carbon-based composite anodes

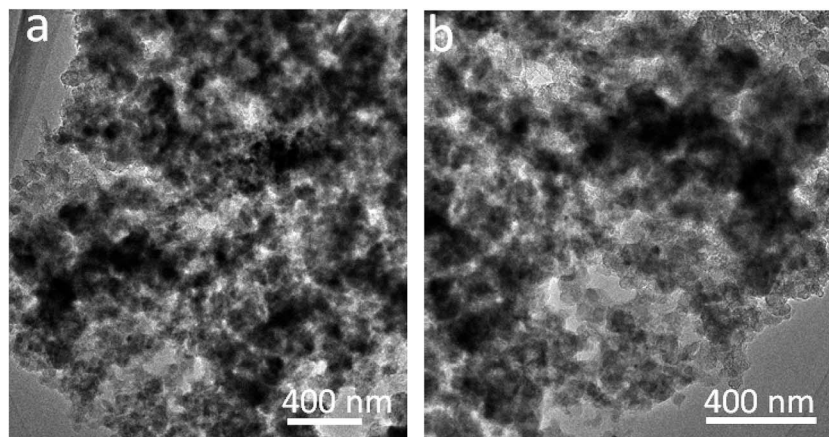| $SnO_2@$carbon-based composite anodes	Current density (A g^{-1})	Initial charge capacity (m Ah g^{-1})	Final capacity/cycle number (m Ah g^{-1})	Capacity retention (%)	Reference
$SnO_2@C$ yolk–shell nanospheres	0.1	1236	630 (100)	51.0	47
Carbon coated SnO_2/graphene	0.1	955	770 (70)	80.6	48
$SnO_2@C$ nanocomposites	0.1	1208	900 (50)	74.5	49
$SnO_2@OMC$	0.05	943	646 (50)	68.5	40
SnO_2 SMCs@C	0.05	1220.3	870.9 (120)	71.4	15
$SnO_3@voids@C$	0.2	1246	986 (50)	79.1	34
SnO_2 NPs@carbon networks	0.1	945	597 (220)	63.2	39
SnO_2 nanotube @C	0.5	947	596 (200)	62.9	50
SnO_2-NPs/EG	0.1	~1160	976 (100)	84.1	45
NSG/CNTs@SnO_2	0.2	1296	1118 (100)	86.3	51
F–G/$SnO_2@C$	0.1	889	820 (100)	92.2	52
$SnO_2@PC1$	0.2	1255	1130 (100)	90.0	**This work**
	0.5	1150	770 (300)	67.0	

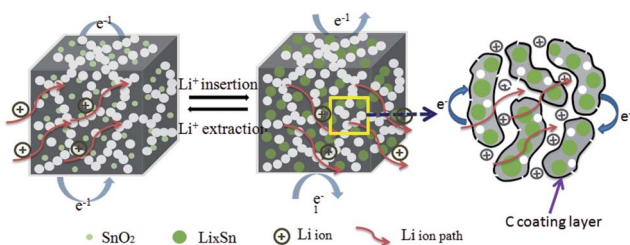Fig. 7   TEM images of SnO$_2$@PC1 before (a) and after (b) 300 cycles.

Fig. 8   A schematic illustration of the Li$^+$ insertion/extraction processes of the SnO$_2$@PC anode.

compared with pure SnO$_2$, indicating the good electrical conductivity of SnO$_2$@PC1. These results altogether demonstrate that porous carbon as a support for SnO$_2$ plays a significant role in improving the electrochemical performance of the SnO$_2$@PC anodes.

To better highlight the generality of the porous carbon structure, the rate capability of the SnO$_2$@PC2, SnO$_2$@PC3, and SnO$_2$@PC4 anodes was tested, as shown in Fig. S9.† At the same rate testing conditions, when the current density was returned back to 0.2 A g^{-1}, the specific capacities of SnO$_2$@PC2, SnO$_2$@PC3, and SnO$_2$@PC4 remained at 921.8, 743.2 and 461.5 m Ah g^{-1}, respectively, which is lower than that of SnO$_2$@PC1. This case proved that a desirable carbon coating layer thickness is a key factor for improving the lithium storage performance of SnO$_2$@PC-based anodes in LIBs, in which the relatively thin carbon shell layer could be destroyed by the repeated volume change, leading to the release of SnO$_2$ active material from the carbon loading layer during the repeated charge–discharge processes. It can also be concluded that the lithium storage performance of SnO$_2$@PCx (x = 2, 3, 4) is inferior compared with SnO$_2$@PC1.

Next, in order to further investigate the structural integrity of the SnO$_2$@PC anodes, the long term cycling performance of SnO$_2$@PC1 at a current density of 0.5 A g^{-1} was examined. The charge specific capacity of SnO$_2$@PC1 could reach up to 770.3 m Ah g^{-1} after 300 cycles, with a capacity retention of 67.0%. For comparison, the cycling performance of the other SnO$_2$@PC-

based anodes was tested, as shown in Fig. S10.† The specific capacities of the SnO$_2$@PC2, SnO$_2$@PC3, and SnO$_2$@PC4 anodes after 200 cycles at 0.5 A g^{-1} were 573.6, 457.1, and 68.3 m Ah g^{-1}, respectively, and their capacity retentions were calculated to be ~51.3, 50.2, and 9.31%, respectively. These electrochemical data are much lower than that of SnO$_2$@PC1 and so these results fully demonstrate that the prepared SnO$_2$@PC1 anode displays optimal lithium storage capability compared with similar SnO$_2$@PCx (x = 2, 3, 4) anodes. Moreover, the cycling and rate performance of the SnO$_2$@PC1 anode in LIBs is superior to most previously reported results in literature, and a detailed performance comparison can be seen in Table 1. Herein, capacity fading occurs in the initial cycling process that may be owing to the partial destruction of the anode structure. The morphology and microstructural changes of the SnO$_2$@PC1 before and after long cycles are shown in Fig. 7 and S11.† After the charge/discharge cycles, the SnO$_2$@PC1 anode material displays a similar structure to the as-synthesized sample, and it was seen that after long cycles the SnO$_2$@PC1 composite structure was not destroyed, but only partly aggregated compared to the fresh sample. The above results indicate that the SnO$_2$@PC1 has a relatively robust structure.

The electrochemical reaction process of Li$^+$ insertion/extraction of the SnO$_2$@PC electrode is illustrated in Fig. 8. The superior cycling and rate performance of the SnO$_2$@PC1 electrode is due to the rational design of the novel carbon coating structure. In this work, the porous carbon plays an important role in enhancing the electrochemical performance. The porous carbon of SnO$_2$@PC offers pathways for fast electron/ion transportation, preventing the pulverization and aggregation of SnO$_2$ nanoparticles and promoting the formation of a stable SEI film, the high SSA of SnO$_2$@PC provides many more active sites for lithium storage to facilitate the transportation of ions and electrons, and the larger pore volume provides extra void space to buffer volume expansion/contraction during the cycling process. The above results and analysis fully demonstrate that effective combination of the high theoretical capacity of SnO$_2$ and the unique porous carbon

coating structure can synergistically enhance the lithium storage performance, especially the cycling and rate capability of the SnO$_2$@PC anode in LIBs.

4. Conclusion

In summary, this work demonstrated that a type of novel porous carbon-coated SnO$_2$-based composite could be successfully produced in the presence of a silica template. The prepared SnO$_2$@PC composite possesses a large specific surface area and a high pore volume, which can significantly shorten the diffusion path of lithium ions and provide a sufficient internal void space for the volume change of SnO$_2$. Benefiting from unique structural features, the prepared SnO$_2$@PC composite anodes exhibit high specific capacity, excellent cycling durability and remarkable rate capability in LIBs. In addition, the synthetic strategy proposed here can be extended to produce similarly structured electrode materials for high-performance LIBs.

Acknowledgements

References

1 V. Etacheri, R. Marom, R. Elazari, G. Salitra and D. Aurbach, *Energy Environ. Sci.*, 2011, **4**, 3243–3262.

2 J. B. Goodenough and Y. Kim, *Chem. Mater.*, 2010, **22**, 587–603.

3 J. B. Goodenough and K.-S. Park, *J. Am. Chem. Soc.*, 2013, **135**, 1167–1176.

4 M. Armand and J. M. Tarascon, *Nature*, 2008, **451**, 652–657.

5 J. M. Tarascon and M. Armand, *Nature*, 2001, **414**, 359–367.

6 L. Liu, F. Xie, J. Lyu, T. Zhao, T. Li and B. G. Choi, *J. Power Sources*, 2016, **321**, 11–35.

7 J. S. Chen and X. W. Lou, *Small*, 2013, **9**, 1877–1893.

8 Q.-H. Wu, C. Wang and J.-G. Ren, *Ionics*, 2013, **19**, 1875–1882.

9 X. W. Lou, L. A. Archer and Z. Yang, *Adv. Mater.*, 2008, **20**, 3987–4019.

10 A. S. Arico, P. Bruce, B. Scrosati, J. M. Tarascon and W. Van Schalkwijk, *Nat. Mater.*, 2005, **4**, 366–377.

11 Y. Chen, J. Ma, Q. Li and T. Wang, *Nanoscale*, 2013, **5**, 3262–3265.

12 K. Zhao, L. Zhang, R. Xia, Y. Dong, W. Xu, C. Niu, L. He, M. Yan, L. Qu and L. Mai, *Small*, 2016, **12**, 588–594.

13 X. W. Lou, Y. Wang, C. Yuan, J. Y. Lee and L. A. Archer, *Adv. Mater.*, 2006, **18**, 2325–2329.

14 X. M. Yin, C. C. Li, M. Zhang, Q. Y. Hao, S. Liu, L. B. Chen and T. H. Wang, *J. Phys. Chem. C*, 2010, **114**, 8084–8088.

15 B. Huang, X. Li, Y. Pei, S. Li, X. Cao, R. C. Massé and G. Cao, *Small*, 2016, **12**, 1945–1955.

16 C. Xu, J. Sun and L. Gao, *J. Mater. Chem.*, 2012, **22**, 975–979.

17 Y. Wang, H. C. Zeng and J. Y. Lee, *Adv. Mater.*, 2006, **18**, 645–649.

18 D. Pham-Cong, J. S. Park, J. H. Kim, J. Kim, P. V. Braun, J. H. Choi, S. J. Kim, S. Y. Jeong and C. R. Cho, *Carbon*, 2017, **111**, 28–37.

19 J. Ye, H. Zhang, R. Yang, X. Li and L. Qi, *Small*, 2010, **6**, 296–306.

20 Y. Zhu, H. Guo, H. Zhai and C. Cao, *ACS Appl. Mater. Interfaces*, 2015, **7**, 2745–2753.

21 Z. Wang, H. Zhang, N. Li, Z. Shi, Z. Gu and G. Cao, *Nano Res.*, 2010, **3**, 748–756.

22 (*a*) L. Pan, K.-X. Wang, X.-D. Zhu, X.-M. Xie and Y.-T. Liu, *J. Mater. Chem. A*, 2015, **3**, 6477–6483; (*b*) D. Zhang, Q. Wang, Q. Wang, J. Sun, L. Xing and X. Xue, *Electrochim. Acta*, 2015, **174**, 476–482.

23 R. Liang, H. Cao, D. Qian, J. Zhang and M. Qu, *J. Mater. Chem.*, 2011, **21**, 17654–17657.

24 L. Cui, J. Shen, F. Cheng, Z. Tao and J. Chen, *J. Power Sources*, 2011, **196**, 2195–2201.

25 R. Liu, D. Li, C. Wang, N. Li, Q. Li, X. Lu, J. S. Spendelow and G. Wu, *Nano Energy*, 2014, **6**, 73–81.

26 C. Botas, D. Carriazo, G. Singh and T. Rojo, *J. Mater. Chem. A*, 2015, **3**, 13402–13410.

27 Y. Deng, C. Fang and G. Chen, *J. Power Sources*, 2016, **304**, 81–101.

28 L. Wang, D. Wang, Z. Dong, F. Zhang and J. Jin, *Nano Lett.*, 2013, **13**, 1711–1716.

29 H. Zhang, H. Song, X. Chen, J. Zhou and H. Zhang, *Electrochim. Acta*, 2012, **59**, 160–167.

30 S. Ding, J. S. Chen and X. W. Lou, *Adv. Funct. Mater.*, 2011, **21**, 4120–4125.

31 C. A. Bonino, L. Ji, Z. Lin, O. Toprakci, X. Zhang and S. A. Khan, *ACS Appl. Mater. Interfaces*, 2011, **3**, 2534–2542.

32 Z. Shen, Y. Hu, Y. Chen, R. Chen, X. He, X. Zhang, H. Shao and Y. Zhang, *Electrochim. Acta*, 2016, **188**, 661–670.

33 M. Dirican, M. Yanilmaz, K. Fu, Y. Lu, H. Kizil and X. Zhang, *J. Power Sources*, 2014, **264**, 240–247.

34 W. Xie, L. Gu, F. Xia, B. Liu, X. Hou, Q. Wang, D. Liu and D. He, *J. Power Sources*, 2016, **327**, 21–28.

35 (*a*) J. Qin, C. He, N. Zhao, Z. Wang, C. Shi, E.-Z. Liu and J. Li, *ACS Nano*, 2014, **8**, 1728–1738; (*b*) L. Xing, C. Ma, C. Cui and X. Xue, *Solid State Sci.*, 2012, **12**, 111–116.

36 Y. Dong, M. Yu, Z. Wang, Y. Liu, X. Wang, Z. Zhao and J. Qiu, *Adv. Funct. Mater.*, 2016, **26**, 7590–7598.

37 W.-M. Zhang, J.-S. Hu, Y.-G. Guo, S.-F. Zheng, L.-S. Zhong, W.-G. Song and L.-J. Wan, *Adv. Mater.*, 2008, **20**, 1160–1165.

38 J. Yang, L. Xi, J. Tang, F. Chen, L. Wu and X. Zhou, *Electrochim. Acta*, 2016, **217**, 274–282.

39 F. Wang, H. Jiao, E. He, S. Yang, Y. Chen, M. Zhao and X. Song, *J. Power Sources*, 2016, **326**, 78–83.

40 H. Xue, J. Zhao, J. Tang, H. Gong, P. He, H. Zhou, Y. Yamauchi and J. He, *Chem.–Eur. J.*, 2016, **22**, 4915–4923.

41 S. M. He, Dissert. Master Degree, China, 2007.

42 L. Wu, J. Yang, X. Zhou, M. Zhang, Y. Ren and Y. Nie, *J. Mater. Chem. A*, 2016, **4**, 11381–11387.

43 S. R. Mukai, T. Hasegawa, M. Takagi and H. Tamon, *Carbon*, 2004, **42**, 837–842.

44 W. Zhang, X. Zhu, X. Chen, Y. Zhou, Y. Tang, L. Ding and P. Wu, *Nanoscale*, 2016, **8**, 9828–9836.

45 Y. Li, Y. Zhao, C. Ma and Y. Zhao, *Electrochim. Acta*, 2016, **218**, 191–198.

46 S.-W. Bian and L. Zhu, *RSC Adv.*, 2013, **3**, 4212–4215.

47 J. Wang, W. Li, F. Wang, Y. Xia, A. M. Asiri and D. Zhao, *Nanoscale*, 2014, **6**, 3217–3222.

48 W. Li, D. Yoon, J. Hwang, W. Chang and J. Kim, *J. Power Sources*, 2015, **293**, 1024–1031.

49 M. Wang, H. Yang, X. Zhou, W. Shi, Z. Zhou and P. Cheng, *Chem. Commun.*, 2016, **52**, 717–720.

50 X. Zhou, L. Yu and X. W. Lou, *Nanoscale*, 2016, **8**, 8384–8389.

51 X. Zhou, L. Xi, F. Chen, T. Bai, B. Wang and J. Yang, *Electrochim. Acta*, 2016, **213**, 633–640.

52 B. Luo, T. Qiu, L. Hao, B. Wang, M. Jin, X. Li and L. Zhi, *J. Mater. Chem. A*, 2016, **4**, 362–367.